# A Raman-based endoscopic strategy for multiplexed molecular imaging

Cristina L. Zavaleta[a,b,c,1], Ellis Garai[b,c,d,e,1], Jonathan T. C. Liu[f], Steven Sensarn[b,c,e], Michael J. Mandella[b,c,e], Dominique Van de Sompel[a,b,c], Shai Friedland[g], Jacques Van Dam[h], Christopher H. Contag[b,c,e,i,2], and Sanjiv S. Gambhir[a,b,c,j,k,l,2]

[a]Department of Radiology, Stanford University, Stanford, CA 94305; [b]Molecular Imaging Program at Stanford, Stanford University, Stanford, CA 94305; [c]Bio-X Program, Stanford University, Stanford, CA 94305; [d]Department of Mechanical Engineering, Stanford University, Stanford, CA 94305; [e]Department of Pediatrics, Stanford University, Stanford, CA 94305; [f]Department of Biomedical Engineering, Stony Brook University, Stony Brook, NY 11794; [g]Division of Gastroenterology and Hepatology, Stanford University, Stanford, CA 94305; [h]Division of Gastroenterology and Hepatology, University of Southern California, Los Angeles, CA 90089; [i]Department of Microbiology and Immunology, Stanford University, Stanford, CA 94305; [j]Division of Nuclear Medicine, Stanford University, Stanford, CA 94305; [k]Department of Bioengineering, Stanford University, Stanford, CA 94305; and [l]Department of Materials Science and Engineering, Stanford University, Stanford, CA 94305

Edited* by Michael E. Phelps, University of California, Los Angeles, CA, and approved April 22, 2013 (received for review December 3, 2012)

**Endoscopic imaging is an invaluable diagnostic tool allowing minimally invasive access to tissues deep within the body. It has played a key role in screening colon cancer and is credited with preventing deaths through the detection and removal of precancerous polyps. However, conventional white-light endoscopy offers physicians structural information without the biochemical information that would be advantageous for early detection and is essential for molecular typing. To address this unmet need, we have developed a unique accessory, noncontact, fiber optic-based Raman spectroscopy device that has the potential to provide real-time, multiplexed functional information during routine endoscopy. This device is ideally suited for detection of functionalized surface-enhanced Raman scattering (SERS) nanoparticles as molecular imaging contrast agents. This device was designed for insertion through a clinical endoscope and has the potential to detect and quantify the presence of a multiplexed panel of tumor-targeting SERS nanoparticles. Characterization of the Raman instrument was performed with SERS particles on excised human tissue samples, and it has shown unsurpassed sensitivity and multiplexing capabilities, detecting 326-fM concentrations of SERS nanoparticles and unmixing 10 variations of colocalized SERS nanoparticles. Another unique feature of our noncontact Raman endoscope is that it has been designed for efficient use over a wide range of working distances from 1 to 10 mm. This is necessary to accommodate for imperfect centering during endoscopy and the nonuniform surface topology of human tissue. Using this endoscope as a key part of a multiplexed detection approach could allow endoscopists to distinguish between normal and precancerous tissues rapidly and to identify flat lesions that are otherwise missed.**

optical | colonoscopy

Early detection is the most effective means of improving prognosis for many patients who have cancer; consequently, the development of new point-of-care diagnostic strategies with sufficient sensitivity and specificity for early cancer detection is critical for effective disease management. Raman spectroscopy has emerged as an excellent analytical tool for multiparameter molecular analyses with both high sensitivity and multiplexing capabilities. These unique features offer the potential for early diagnosis, which could have a significant impact on the survival rates of patients with cancer.

Raman spectroscopy is based on an inelastic light-scattering phenomenon that provides detailed chemical information, but biomedical applications have been limited by very low signal-to-noise ratios. Most photons are elastically scattered when they interact with matter, where the scattered photons maintain the same energy and wavelength as the incident photons. However, a very small fraction of light is inelastically scattered, meaning that the linearly inelastic scattered photons usually lose energy, resulting in a longer wavelength. This inelastic scattering of light was first observed in 1928 by C. V. Raman and is now termed spontaneous Raman scattering (1). Since then, Raman spectroscopy has been predominantly used as an analytical tool to determine the molecular composition of materials based on the energy differences observed between the incident and scattered photons. However, more recently, researchers have used Raman spectroscopy to interrogate various biomedical processes, such as the analysis of cells in culture, excised tissue samples, and preclinical animal models, and, more recently, to perform clinical diagnosis (2–11).

Researchers have attempted to use Raman spectroscopy for clinical diagnosis by interrogating the intrinsic chemical differences between malignant and normal tissues (5). However, the inefficiency associated with intrinsic Raman scattering remains a significant limitation for early diagnosis because it often leads to poor signals, long exposure times, and less than adequate sensitivity for the subtle changes associated with early-stage cancer as a result of the lack of photons. This inefficiency, along with limited depth of penetration, has severely limited translation of Raman spectroscopy into the clinic.

We have developed a unique clinical diagnostic strategy that addresses both of the major limitations to effective in vivo Raman-based imaging. First, we can overcome the inefficiency of Raman scattering by using surface-enhanced Raman scattering (SERS) nanoparticles as tumor-targeting contrast agents (10, 12, 13). These gold-based nanoparticles exhibit a plasmon resonance effect on their encapsulated metallic surface that dramatically increases the Raman scattered light emitted by small molecules adsorbed onto the surface (14). These small molecules represent the Raman-active layer that results in a unique spectral fingerprint, allowing for multiple "flavors" of SERS nanoparticles to be used simultaneously for multiplexing. In addition, to address some of the limitations of detection, we have developed a small, flexible, fiber optic-based Raman device (5-mm diameter) that enables noncontact detection of Raman signals. This device has been carefully designed with the goal of it being inserted through the accessory channel of a clinical endoscope, enabling physicians

Author contributions: C.L.Z., E.G., J.T.C.L., S.S., M.J.M., J.V.D., C.H.C., and S.S.G. designed research; C.L.Z., E.G., J.T.C.L., S.S., D.V.d.S., and S.F. performed research; C.L.Z., E.G., and D.V.d.S. analyzed data; and C.L.Z., E.G., C.H.C., and S.S.G. wrote the paper.

The authors declare no conflict of interest.

*This Direct Submission article had a prearranged editor.

Freely available online through the PNAS open access option.

[1]C.L.Z. and E.G. contributed equally to this work.

[2]To whom correspondence may be addressed. E-mail: ccontag@stanford.edu or sgambhir@stanford.edu.

See Author Summary on page 10062 (volume 110, number 25).

This article contains supporting information online at www.pnas.org/lookup/suppl/doi:10.1073/pnas.1211309110/-/DCSupplemental.

to gain access to tissues of interest not accessible with other optical devices for molecular analyses. After introducing these tumor-targeting nanoparticles into the gastrointestinal tract, physicians would have access to unique functional information associated with this Raman-based strategy to localize cancer better and improve early detection during endoscopic, laparoscopic, or surgical procedures, as well as obtaining important molecular information that could guide follow-up therapy.

Endoscopy has become an important tool in visually assessing structural details deep within the body. Several organs are easily accessible with endoscopic tools, including the bladder (cystoscopy), cervix (colposcopy), lung (bronchoscopy), esophagus and stomach (upper gastrointestinal endoscopy), and, most notably, the colon (colonoscopy). It is well known that screening and treatment of polyps via endoscopy could prevent the majority of colorectal cancers (~80%) and significantly decrease the mortality rate due to colorectal cancers (15, 16). However, white-light endoscopy alone is an imperfect technology that only offers structural details based on visual observation and can result in miss rates of up to 25% (16). It was also reported that flat lesions in the colon, which are more difficult to detect with white-light endoscopy, were fivefold more likely to contain cancerous tissue than the visually apparent polyps detected by conventional colonoscopy (17). This problem of failed detection could be significantly minimized with the addition of a molecular imaging component that reveals important functional information in conjunction with the structural component that white light endoscopes offer today.

In this paper, we discuss the fabrication and characterization of a fiber optic-based Raman endoscope that has the capability to detect and quantify the presence of a single or multiplexed panel of tumor-targeting SERS nanoparticles. This Raman endoscope is a principal component in the development of our functional imaging strategy, which involves the following: (*i*) topical administration of tumor-targeted SERS nanoparticles to a particular area of interest during endoscopy followed by washing of the unbound SERS nanoparticles, (*ii*) utilization of our Raman endoscopic device as it is deployed through the working channel of a commercial endoscope to detect and quantify the presence of the bound targeted SERS nanoparticles relative to internal controls, and (*iii*) interpretation of results in real-time to determine what pathological conditions exist based on the identified location and types of bound SERS nanoparticle flavors. In this study, we have thoroughly assessed the usability and capability of our newly developed Raman endoscope to detect and multiplex an array of SERS nanoparticles within phantoms and on excised tissue samples. We have reported previously on functionalization of the SERS nanoparticles (12, 13, 18); although regulatory approval is pending for the topical administration of these particles in the human colon, we have been able to evaluate our Raman endoscope design extensively in patients. To advance this technology further and demonstrate the capability of the Raman endoscope, we simulated Raman signals by superimposing separately measured SERS spectra onto the intrinsic Raman signals obtained from patients during endoscopy.

Various parameters relating to the in vivo detection of SERS nanoparticles with the Raman endoscopic device were evaluated to determine its suitability for clinical use, including reproducibility, sensitivity, depth of penetration, maximum permissible exposure (MPE), working distance, and spectral unmixing. Additionally, extensive multiplexing experiments were performed to test the limits of our system's ability to unmix multiple spectra from various batches of SERS nanoparticles. Finally, with the approval of the Stanford Institutional Review Board (IRB), we evaluated in a pilot study the performance and usability of the Raman endoscope component in humans during routine colonoscopy. The data presented here indicate that these tools comprise a supporting technology that may enable physicians to obtain unique molecular information with Raman spectroscopy that may help guide endoscopic, laparoscopic, and surgical procedures.

## Results

**SERS Raman Nanoparticles.** The experiments performed in this study used SERS nanotags (Cabot Security Systems, formerly Oxonica Materials, Inc.) (19, 20). These Raman nanoparticles consist of a unique Raman-active layer adsorbed onto a 60-nm gold core and then coated with silica, resulting in an effective diameter of ~120 nm. To demonstrate multiplexing, we used 10 different SERS nanoparticle flavors, each consisting of a unique Raman-active layer and a unique spectral fingerprint (*SI Appendix*, Fig. 1). We have described the molecular composition of these Raman-active layers previously (21). After excitation with a 785-nm laser, these SERS nanoparticles display a distinct spectrum based on the interaction of the incident light with the unique Raman-active layer adsorbed onto the gold core. The gold core acts as a surface field enhancer and can increase the effective Raman scattering efficiency by several orders of magnitude, which allows for ultrasensitive detection and makes it ideal for early detection diagnostic screening over large fields of view (14). Because the penetration of light is severely limited in tissues, we intend to integrate Raman imaging into an endoscopic instrument to access epithelial surfaces at clinically relevant depths within the body.

**Design and Fabrication of Raman Endoscope.** The Raman endoscopic device uses a flexible fiber bundle with a centrally located single-mode fiber for illumination at 785 nm and an additional 36 surrounding multimode fibers for light collection. A singlet lens is used for dual purposes: to collimate the outgoing illumination beam and to collect the incoming SERS signals onto the multimode fibers. This collimating lens (6-mm focal length, 4-mm diameter) produces an illumination spot of ~1 mm in diameter (Fig. 1*A*; more details are provided in *SI Appendix, Collimating Beam*). A unique feature of our Raman endoscope, as opposed to others already used clinically, is that ours is not a contact probe and has been specifically designed for efficient use, and signal uniformity, over a wide range of working distances, ranging from 1 to 10 mm, that are relevant for colonoscopy. This is necessary to accommodate user variability and imperfect centering during endoscopy, as well as the nonuniform surface topology of human tissue (*SI Appendix, Working Distance*). The circular honeycomb pattern of multimode fibers has been rearranged into a linear array at the proximal end of the fiber bundle, which is coupled into a spectrometer (RamanSpec RS-780; BaySpec) by aligning the linear array with the entrance slit (Fig. 1*B*, *Inset*). The spectrometer disperses the light collected by each multimode fiber, and the vertical slit is imaged onto a cooled, deep-depletion CCD array (DU920P-BR-DD; Andor Technologies) (Fig. 1*C*). The CCD then performs full vertical binning (FVB) of the sensor array to sum the spectral intensity of the collected light from all the collection fibers at each wavelength. Once an FVB acquisition is obtained for a given exposure time, the acquired signal is decomposed, using a direct classical least squares (DCLS) algorithm (*Methods, DCLS-Weighting Factors*), into weighting factors that quantify the intensities of the Raman-scattered signals as fractions of previously measured reference spectra.

The Raman endoscopic device designed for colon cancer detection has an external diameter of 5 mm (Fig. 1*A*) and is capable of being deployed through the instrument channel (6-mm internal diameter) of a clinical endoscope (GIF-XT30; Olympus). A major design challenge was to ensure that the Raman endoscope device fits inside the accessory channel of a conventional endoscope without damaging the optics. Most conventional endoscopes have an angular bend at the opening of the accessory working channel that requires the rigid length of the accessory to be short; it was imperative for the Raman endoscope to meet this particular design restriction (*SI Appendix*, Movie S1).

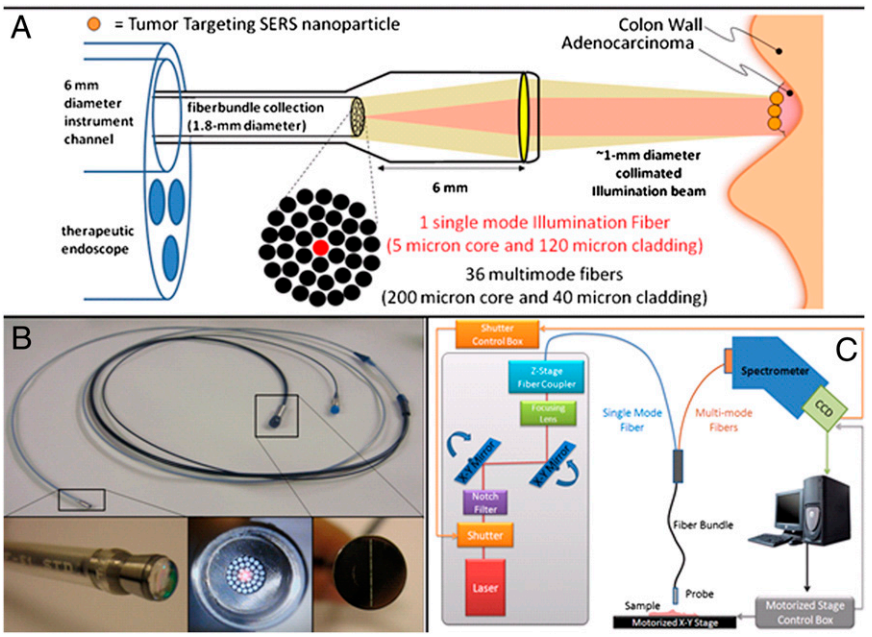


**Fig. 1.** Raman endoscope design and setup. (*A*) Schematic of Raman endoscope designed to be inserted through the accessory channel of a clinical endoscope with a 6-mm instrument channel. The Raman endoscope is composed of a single-mode illumination fiber that is surrounded by a bundle of 36 multimode collection fibers, totaling a diameter of 1.8 mm. The excitation laser light is collimated by a lens to emit an illumination spot size of ~1.2 mm. (*B*) Photograph depicts the final fabricated Raman endoscope to be used for clinical studies. (*Lower*) Enlarged digital photograph of the endoscope head (Left), a magnified photograph of the fiber bundle (*Center*), and a magnified photograph of the back end of the device (*Right*) show a linear array of the 36 collection fibers that are specially aligned to fit into a spectrometer. (*C*) Schematic of the entire device setup starting with the 785-nm laser whose output is controlled by a shutter driven by a computer-driven shutter controller. The laser is then passed through a notch filter, which ensures a narrow 785-nm bandwidth, is guided through a series of mirrors, and is refocused to a single-mode fiber to illuminate a sample. The light collected by the multimode fibers is dispersed by wavelengths onto a CCD via a spectrometer.

The current setup consists of a 785-nm laser that passes through a notch filter, two angularly adjustable mirrors, an electromechanical shutter, and a focusing lens to couple the laser (*SI Appendix, Laser Coupling*) into the single-mode illumination fiber (Fig. 1*C* and *SI Appendix*, Fig. 2). The electromechanical shutter (P/N:SH05; ThorLabs) is activated by a shutter control box (P/N: SC10; ThorLabs). The shutter is programmed only to open when the shutter controller receives a trigger signal from the CCD to acquire a signal. It is important that the shutter defaults to the closed position so that the exposure time of the laser to the tissue surface, for a given power and spot size, remains under the American National Standards Institute (ANSI) MPE (*SI Appendix, ANSI MPE* and Table 1). The notch filter is placed between the continuous-wave laser source and the single-mode fiber to eliminate broadband noise, including amplified spontaneous emission, from the laser. The maximum achievable power output from the distal end of the device is 42 mW (*SI Appendix, Laser Characterization*).

Our custom spectrometer was designed to have an N.A. of 0.28 to match our fiber bundle and CCD array requirements (*SI Appendix, Spectrometer*). The spectrometer has a wavelength range of 830–930 nm and includes an 840-nm long-pass filter to remove scattered incident laser light. The spectral resolution for the spectrometer system is ~1 nm and resolves Raman transitions from 700 to 2,000 $cm^{-1}$. The spectral resolution was determined using a low-pressure mercury discharge lamp, which has distinct emission lines within the wavelength range that our spectrometer is able to detect.

**Characterization.** The power output of the Raman endoscope was first monitored to determine its stability. The device's power output was shown to be stable over varying working distances of up to 25 mm away from the sample surface; this was demonstrated at different power settings (Fig. 2*A*). The variation of the power output, measured over 1 min, was less than 0.13% when measured at 15 mW and a fixed working distance. The percentage variation was lower at a higher power level of 42 mW (*SI Appendix*, Table 2).

By performing FVB of the SERS signals dispersed onto the CCD array and using the DCLS algorithm, we were able to obtain reproducible Raman spectra with integration times as short as 1 ms successfully. The reproducibility, measured in terms of the coefficient of variance, further improved for integration times of 10 ms or greater (Fig. 2*B* and *SI Appendix, Signal Stability*). Additionally, we confirmed that the Raman signal increases linearly with laser power (*SI Appendix*, Fig. 3). The majority of the experiments conducted in these studies used either a laser output power of 15 mW with a 1-s CCD acquisition time or a laser output power of 42 mW with a 300-ms acquisition time. These settings were selected to stay within the ANSI MPE limits (*SI Appendix, ANSI MPE* and Table 1).

The collection efficiency of the multimode fibers in the Raman probe is relatively constant for working distances between 0 and 10 mm (Fig. 2*C*). In that range, the multimode fibers are being efficiently used for light collection, as verified using ZEMAX (Radiant Zemax, LLC) optical ray-tracing software (*SI Appendix*, Fig. 4). As the working distance continues to increase beyond 10 mm, the collection efficiency begins to drop as $\frac{1}{d^2}$, where $d$ is the working distance between the distal end of the device and the tissue surface with or without Raman nanoparticles (*SI Appendix, Working Distance*). Even at large working distances, Raman signals were still identifiable (e.g., 40 mm away from the sample surface, which is well beyond the required working distance for applications within the colon). This trend was validated on Raman nanoparticles placed on a quartz slide (*SI Appendix*, Fig. 5), as well as on human colon tissue biopsies as seen in Fig. 2*C*.

To evaluate how deep below the surface of tissue the nanoparticles can be imaged, a bench-top phantom was created. The phantom was composed of an agarose solution with similar absorption and scattering properties as the colon tissue (*Methods, Depth Study*). Using this phantom, a depth of penetration of 4.5 mm was achieved using 42 mW of laser power and 300 ms of acquisition time; using 15 mW and 1 s, respectively, a depth of penetration of 5 mm was achieved (Fig. 2*D*). More detailed information is provided in *Methods* (*Defining Thresholds* and *Statistical Analysis*).

SERS particles can be engineered to emit different spectral signatures or flavors. For a single SERS particle flavor (e.g., S440) and a fixed working distance, laser power, integration time, and SERS particle volume, it was demonstrated that the mean Raman weighting factor was linearly proportional to the concentration when the nanoparticles were placed in a well plate (Fig. 2*E*), on a quartz slide (*SI Appendix*, Fig. 6 *A* and *B*), on ex vivo porcine colon tissue (*SI Appendix*, Fig. 6 *C* and *D*), and on human colon

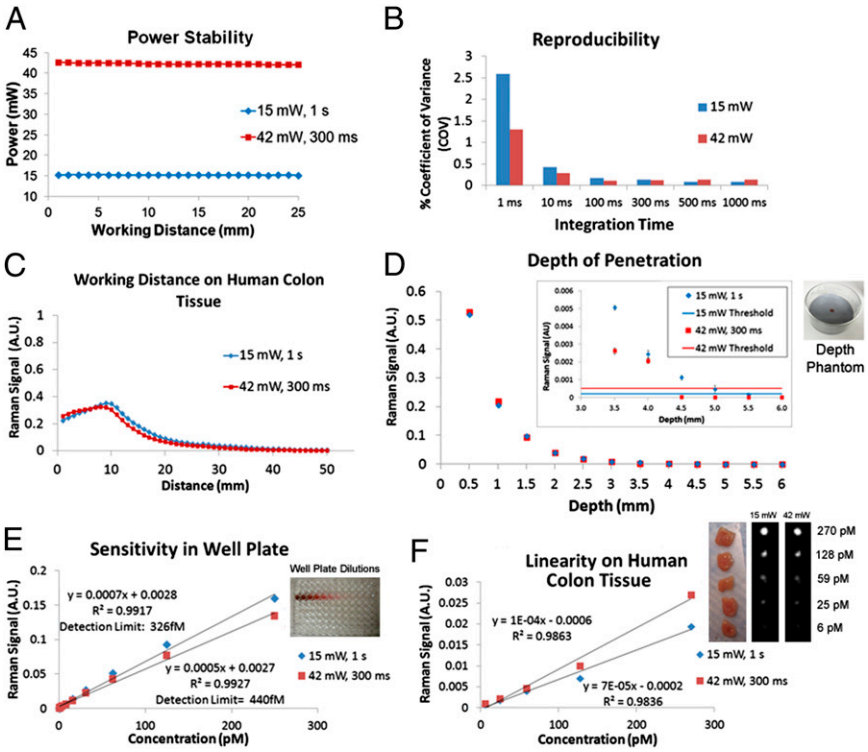


**Fig. 2.** Characterization of Raman endoscope performance. (*A*) Power output stability over a working distance of 25 mm away from sample surface. (*B*) Raman signal reproducibility of the Raman endoscope device over several integration times. Shorter integration times lead to more variability in signal; however, even at 1-ms integration times, the reproducibility is still good with a coefficient of variance (COV) of only ~2.5%. (*C*) Raman signal is stable over a working distance of 10 mm away from sample surface. The signal drops off ($1/d^2$) after the Raman endoscope is more than 10 mm away from the sample due to the solid angle collection efficiency. A.U., arbitrary units. (*D*) Raman endoscope device was able to detect Raman signal above the background threshold level at a depth of 4.5 mm when using 42 mW and a 300-ms integration time and at a depth of 5 mm when using 15 mW with a 1-s integration time in our tissue-mimicking phantom (*Right*). The phantom was fabricated in-house and was prepared to have similar scattering and absorption properties as human colon tissue. (*E*) Correlation of the Raman signal to concentration of S440 in a well plate using the Raman endoscope device. The limit of detection was 326 fM (15 mW at 1 s) and 440 fM (42 mW at 300 ms) of SERS nanoparticles in a well plate (*Right*). The SERS Raman concentration correlates linearly with Raman signal at both laser powers. (*F*) Linear correlation of the Raman signal to concentration after topically applying diluted concentrations of S440 onto fresh human colon tissue samples (*Right*). The Raman signal linearly correlates with the concentration of SERS nanoparticles applied.

biopsies (Fig. 2*F*). Bench-top experiments using 300 μL of SERS S440 particles placed in a well plate have shown the ability to detect 440 fM SERS particles with a laser illumination of 42 mW, integration time of 300 ms, and working distance of ~5 mm. This corresponds to a detection limit of 1.3 million nanoparticles, or ~230 nanoparticles per cell, for an average cell cross-section of 100 $\mu m^2$ (*SI Appendix, Detection Limit Calculation*). At a laser illumination of 15 mW and a longer integration time of 1 s, we were able to detect as little as a 326-fM concentration of SERS particles. More details are provided in *Methods* (*SERS Concentration Assessment*, *Mapping and Image Processing*, and *Well Plate Experiment*) and in *SI Appendix*, Fig. 7.

**Multiplexing Experiments.** ***Multiplexing on a quartz slide.*** All multiplexing studies performed herein were evaluated at two different power settings: 15 mW at 1 s per spectral acquisition and 42 mW at 300 ms per spectral acquisition. Due to space constraints, we have reported all the studies performed at 15 mW in *SI Appendix*. To evaluate our Raman endoscope device's initial ability to identify and unmix spectra from various SERS nanoparticles correctly, we first placed 10 separate 3-μL samples of each SERS flavor onto a quartz slide. We then mapped the quartz slide containing the 10 individual drops using 1-mm *x*/*y* translations at times of either 1 s per spectral acquisition using 15 mW (*SI Appendix*, Fig. 8) or 300 ms per spectral acquisition using 42 mW (Fig. 3*A*). The map was analyzed with our postprocessing software, where preassigned reference spectra of each SERS nanoparticle flavor were used to determine the best spectral fit to the measurements in the map. The software sent the intensity maps into 10 separate channels, revealing where in the map each SERS nanoparticle flavor was detected. The resulting image shows all 10 drops correctly separated into their corresponding spectral channel with minimal cross-talk between the channels (Fig. 3*A*).

Next, we assessed the ability of our Raman endoscope device to unmix two colocalized flavors of SERS nanoparticles spectrally. The most abundant flavor we had available was S440; therefore, we mixed equal concentrations of S440 with each of the rest of the nine spectrally unique batches. The resulting intensity maps correctly unmixed each of the nine mixtures containing equal concentrations of S440 and one other SERS flavor (Fig. 3*B*).

We then demonstrated the ability of our Raman endoscope device to unmix colocalized mixtures of 4, 6, 8, and all 10 SERS nanoparticles successfully at equal concentrations (Fig. 3*C*). After successfully demonstrating colocalized multiplexed imaging with all 10 SERS nanoparticles, we assessed various mixtures of nanoparticles at varying concentrations. Before deciding which nanoparticle flavors to mix first and at what concentrations, we calculated which SERS spectra were most distinct relative to that of our most abundant flavor, S440, to have the most success with unmixing the spectra. It was determined that S440, S481, S420, and S421 had the most distinct spectra with very little spectral overlap with S440, and each performed very well with one other at varying concentrations. Fig. 3*D* shows a quantitative linear relationship between each of the SERS nanoparticle concentrations and Raman signal ($R^2$ = 0.9987 at 42 mW).

***Multiplexing on human colon tissue.*** Because our strategy involves a topical application of these SERS nanoparticles onto human tissue for functional tumor-targeting assessment, we evaluated the ability of our Raman endoscope device to multiplex on fresh human colon tissue samples. Each of the 10 nanoparticle flavors was topically applied to fresh human colon tissue samples, and the images revealed a clear distinction between each of the channels with minimal cross-talk (Fig. 4*A*). Furthermore, equal concentrations of the four most distinct SERS flavors (S440, S481, S420, and S421) were mixed together to assess colocalized multiplexing on human colon tissue, and all four were correctly unmixed in their respective channels (Fig. 4*B*). Finally, each of these four SERS flavors were mixed together at varying concentrations and topically applied to fresh human colon tissue to reveal a consistent linear correlation between Raman signal and SERS nanoparticle concentration ($R^2$ = 0.980 at 42 mW) (Fig. 4*C*). More information about the 15-mW human multiplex data is provided in *SI Appendix*, Fig. 9. Therefore, it was determined that the in-

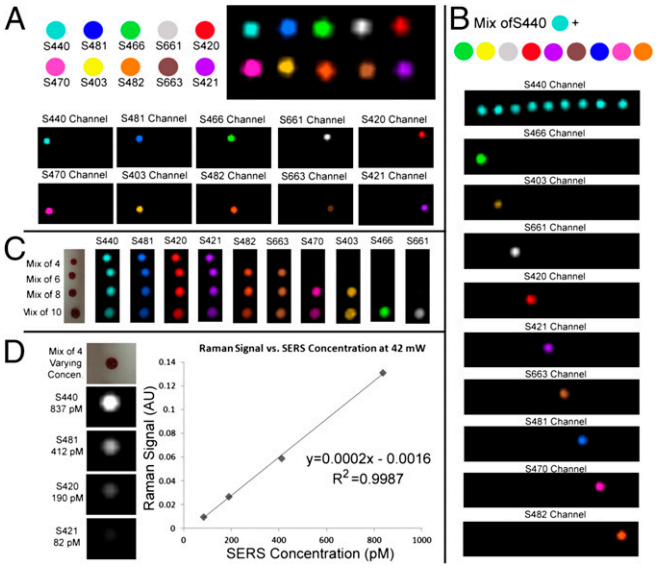


**Fig. 3.** Demonstration of multiplexing on quartz slide at 42 mW. (*A*) Ten unique flavors of SERS nanoparticles spatially separated onto a piece of quartz. The Raman map acquired identifies all 10 flavors correctly. Notice how each of the flavors is correctly represented in each of the SERS nanoparticle channels in the panels below. (*B*) Equal mixture of S440 and one other flavor is placed in separate drops across a piece of quartz to characterize dual colocalization of SERS nanoparticles. The Raman map correctly identifies the presence of each of the 2 flavors of SERS nanoparticles in each mixed droplet as shown in the separate SERS channels below. (*C*) Demonstration of multiple colocalized SERS flavors, including mixtures of 4, 6, 8, and all 10 SERS nanoparticles within the same droplet on quartz. The Raman maps shown depict the correct location of each of the SERS flavors within each of the mixtures. (*D*) Mixture of 4 SERS nanoparticle flavors, each at varying concentrations. The postprocessing software was able to separate each flavor spectrally into its respective channel correctly, and the Raman maps (*Left*) show a decrease in Raman intensity that correlates with the concentrations of each of the SERS flavors. (*Right*) Graph depicts a linear correlation between the SERS concentration of each flavor and the Raman signal, with an $R^2$ value of 0.9987.

trinsic background signal from human colon tissue itself did not interfere with the ability of our Raman endoscope device to multiplex effectively in any significant way.

**Blinded Study: "Scavenger Hunt."** The purpose of this blinded study was to determine the sensitivity and accuracy of the multiplexed system when put in the hands of a user to detect multiple SERS nanoparticle flavors and mixtures at various concentrations. To conduct this study, a porcine colon was splayed open and a 6 × 10 grid, consisting of 60 boxes, was created on the tissue using suture material (Fig. 5*A*). Each box was assigned either zero, one, two, three, or four flavors of colocalized SERS particles at a concentration of ~1 nM. The user was blinded as to what combination of particles was present, if any, in each grid. Within the empty boxes in which no SERS nanoparticles were assigned, a red food dye was placed to ensure that the user was blinded to the presence of the particles. The combinations were randomly generated with a probability that 15–30% of the grid would consist of blanks. The Raman device was mounted in-line with an off-the-shelf semi-flexible boroscope (DCS 100; General) to provide the white-light, real-time video guidance (Fig. 5*B*). The boroscope consisted of a CCD, which transmitted images wirelessly to the computer, and two white-light light-emitting diodes; this was used to help the user navigate over the samples (*SI Appendix*, Movie S2). Three users were tested in this blind study. A representative graph from each user shows the presence of each SERS flavor within each of the 60 boxes (*SI Appendix*, Fig. 10). There was a 99% average user accuracy to the presence of the correct combination of SERS nanoparticle flavors, after using a 7× SD threshold (Fig. 5*C*). The threshold was defined as a multiple of the SD of the background weighting factor, which was added to the mean background weighting factor. No false-negative results were identified throughout the study; therefore, the results were 100% sensitive to the presence of SERS particles across the three users. Additionally, a 96% average specificity was achieved between the three users after applying a 7× SD threshold (Fig. 5*C*). More details regarding the threshold calculation are provided in *Methods* (*Defining Thresholds*). Note that these results reflect the use of SERS nanoparticles at concentrations of ~1 nM in volumes of 3 μL for

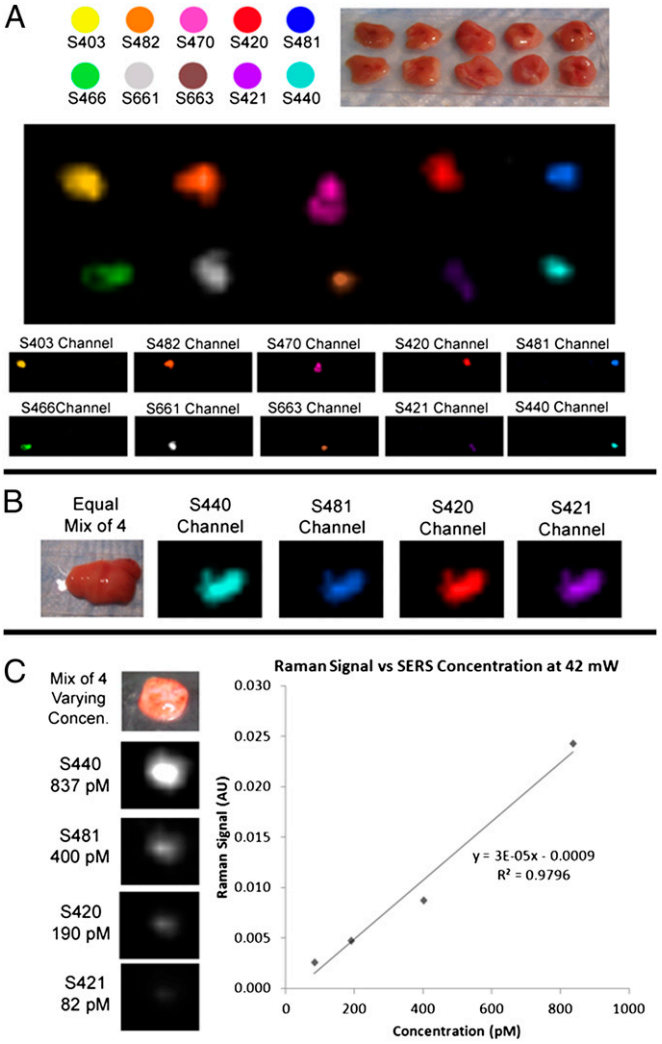


**Fig. 4.** Demonstration of multiplexing on human tissue at 42 mW. (*A*) Ten unique flavors of SERS nanoparticles spatially separated onto 10 separate pieces of fresh human colon tissue. The Raman map acquired identifies all 10 flavors correctly. Notice how each of the flavors is correctly represented in each of the SERS nanoparticle channels in the lower panels. (*B*) Demonstration of colocalized multiplexing, where 4 SERS flavors were equally mixed and applied on a single piece of human colon tissue. The postprocessing software was able to separate each flavor spectrally into its respective channel correctly as shown in the Raman maps (*Right*). (*C*) Mixture of 4 SERS nanoparticle flavors, each at varying concentrations (Concen.), was combined and applied to a single piece of human colon tissue. The postprocessing software was able to separate each flavor spectrally into its respective channel correctly. (*Left*) Raman maps show a decrease in Raman intensity that correlates with the concentrations of each of the SERS flavors. (*Right*) Graph depicts a linear correlation between the SERS concentration of each flavor and the Raman signal, with an $R^2$ value of 0.9796.

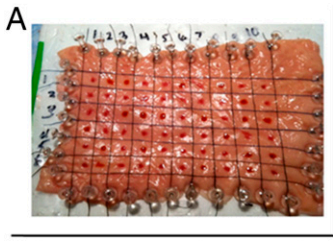


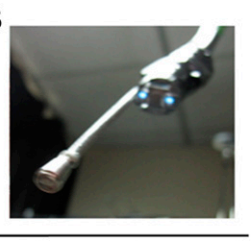


C

| Threshold Multiple | 3x | 5x | 6x | 7x |
|---|---|---|---|---|
| n | 180 | 180 | 180 | 180 |
| True Positive + True Negative | 136 | 166 | 173 | 178 |
| Sensitivity | 100% | 100% | 100% | 100% |
| Specificity | 50% | 76% | 86% | 96% |
| Accuracy (CR) | 76% | 92% | 96% | 99% |
| Mis-CR | 24% | 8% | 4% | 1% |

**Fig. 5.** Scavenger hunt to demonstrate Raman endoscope usability in conjunction with multiple SERS nanoparticles on tissue. (*A*) Pig colon tissue configured into a 6 × 10 grid, where users would interrogate each of the 60 squares with the Raman endoscope. Each square was randomly assigned an unknown mixture of SERS nanoparticles, and some squares had no SERS nanoparticles present. (*B*) Digital photograph of the Raman endoscope setup. Notice how the Raman endoscope is attached to a white light boroscope to help guide the user during the scavenger hunt. (*C*) Statistical averages across the three blinded users are shown in the table. Because there were no *FN* results, regardless of the threshold level, 100% sensitivity was achieved. The average user accuracy, also referred to as the *CR*, is shown as well.

each flavor used and that the sensitivity and specificity would presumably change at lower concentrations closer to the limit of detection (subpicomolar). However, to demonstrate the usability and multiplexing capabilities of the Raman endoscope, we chose a dose of ~1 nM, which has been shown to be nontoxic when administered locally to the colon in mice (18, 22) The sensitivity and specificity were also determined for each SERS flavor combination. More information is provided in *Methods* (*Statistical Analysis*) and *SI Appendix*, Fig. 11.

**Pilot Clinical Study.** Currently, an IRB protocol has been approved for our Raman device, but the SERS nanoparticles will require further regulatory approval. Therefore, the device alone was evaluated in patients to detect intrinsic Raman signals as potential background for future studies (Fig. 6 *A* and *B* and *SI Appendix*, Movie S3). The purpose of this study was to analyze the variability of the background signals in vivo from the colon wall and the usability of our device.

Three male patients undergoing routine screening via colonoscopy consented to participate in this study and were tested with the Raman device by an experienced endoscopist (S.F.). Most endoscopes use a xenon short-arc lamp as the light source, and in our clinical studies, the tower model was an Olympus Evis Exera CLV-180, which uses a 300-W xenon short-arc lamp. The xenon lamp has emission lines in the near IR within our region of interest and contributes to our measured background spectra. The intensity of the lamp, as detected by our endoscope, varies independent of the endoscope's inherent background signal originating from the laser. By inputting reference signals with the lamp source turned on and off into the DCLS algorithm, we can account for these variations. The robustness of the DCLS algorithm to account for background variation and its ability to cancel out the background signal effectively were assessed in datasets acquired in three patients. For patients 1 and 3, at 15 mW of laser power and 1 s of integration time, the residual signal after background cancellation was 0 ± 35 counts (Fig. 7 *A* and *B*). Details are provided in *SI Appendix* (*Clinical Background Cancellation*), and results for all three patients are shown in *SI Appendix* (Fig. 12). When more than one signal from the lamp source was used as a reference in the DCLS algorithm, the background subtraction improved. There are a finite number of additional backgrounds in which a noticeable improvement occurs, after which there is only incremental benefit from adding additional background references to the DCLS algorithm (*SI Appendix*, Fig. 12*E*).

Because we were unable to administer our SERS nanoparticles in patients, we simulated Raman signals by superimposing separately measured SERS spectra onto our in vivo patient data. The SERS spectra were obtained by administering diluted S440 nanoparticles onto excised human colon tissue and sampling the spectra with our device. After background subtraction, these spectra were added to our patient acquisitions (in all three patients with the lamp source either on or off) and the DCLS algorithm was used to extract the simulated signal (Fig. 7 *C*–*F*). For these simulations, nanoparticle concentrations of 270, 128, 59, 25, and 6 pM were used (*SI Appendix, Clinical SERS Simulation* and Figs. 13–20 for all three patient datasets with the lamp source either on or off). The Raman signal extracted from the superimposed in vivo data were larger than the background level, and as little as 6 pM was detected in all patients and scenarios (Fig. 7 *G* and *H* and *SI Appendix*, Figs. 13–20). This demonstrates that once the SERS nanoparticles are approved for use in patients, the Raman device would likely be successful at identifying the particles at low concentrations; moreover, our Raman device is capable of doing so even in the presence of additional background noise, such as the xenon lamp.

## Discussion

Several optical-based endoscopic imaging techniques are currently being explored to enhance colorectal cancer detection, including fluorescence endoscopy, light-scattering spectroscopy, optical coherence tomography, chromoendoscopy, and confocal fluorescence microendoscopy (16, 23, 24). Although these enhanced imaging technologies have proven to be clinically useful for the detection of early cancers and premalignant colon lesions, most rely on visually assessing structural details on the colon wall, although, at present, providing little to no functional information. Some techniques look at basic tissue architecture through fluorescence or characterization of crevices and concave areas with the use of chromogenic dyes, whereas other techniques focus on microscopic subcellular structural changes between normal and dysplastic lesions (24). Other researchers have recognized the importance of adding a functional component to guide endoscopy by using molecularly targeted fluorescent probes, which have shown success in both mouse models and humans (25–27). Although these techniques have great potential to improve the endoscopic detection of pathological conditions in the colon, these fluorescence-based techniques cannot offer the multiplexing capabilities of our nanobased Raman endoscopy strategy.

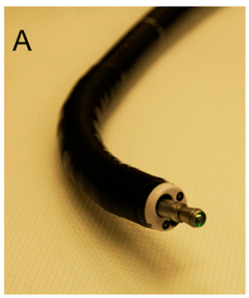


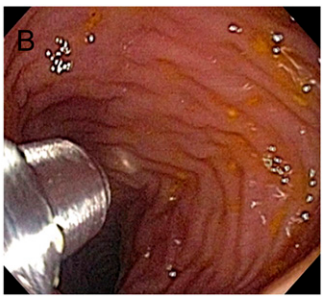


**Fig. 6.** Clinical application and utility of the Raman endoscope in patients. (*A*) Raman endoscope inserted into the instrument channel of a conventional clinical endoscope. (*B*) Digital photograph taken from the white-light endoscopy component of the clinical endoscope portraying our Raman endoscope protruding from the instrument channel and illuminating a spot on the colon wall in a human patient.

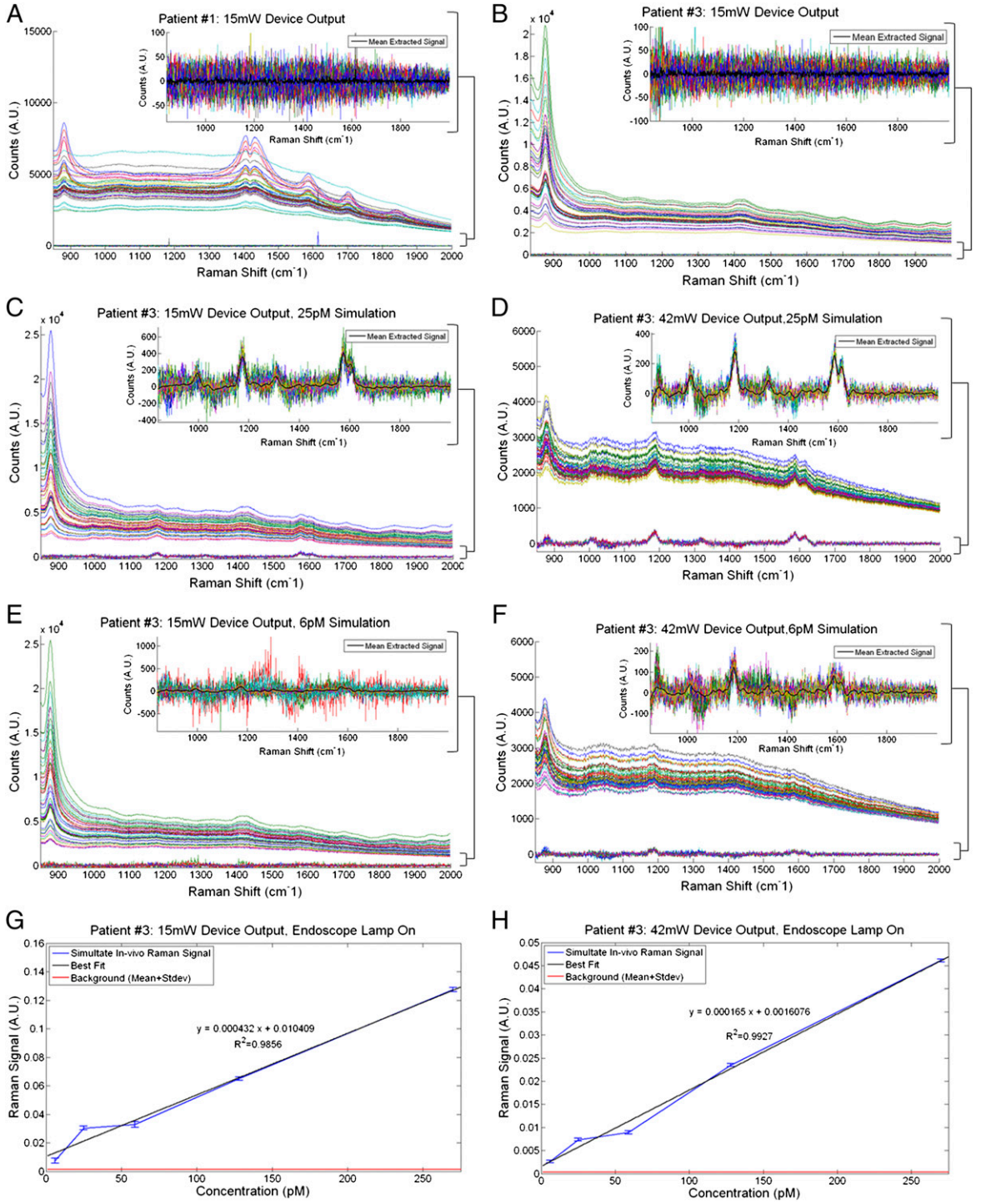


**Fig. 7.** Characterization of Raman endoscope performance in humans. (*A*) In vivo background signals; the peaks are due to the endoscope light source. Ninety background acquisitions were obtained from patient 1 at 15 mW and 1 s. (*Inset*) Residual signal after DCLS background cancellation was 0 ± 35 counts. (*B*) In vivo background signals; the peaks are due to the endoscope light source. The light source unit from patient 3 was different from that of patient 1. Ninety background acquisitions where obtained from patient 3 at 15 mW and 1 s. (*Inset*) Residual signal after DCLS background cancellation was 0 ± 35 counts. (*C*) In vivo Raman signals were simulated by superimposing diluted SERS signals acquired on human tissue with the in vivo background signals. The figure shows the superimposed data from patient 3 at 15 mW and 1 s as well as a SERS signal acquired at a concentration of 25 pM on human tissue. (*Inset*) Extracted SERS signal after DCLS background cancellation. The mean extracted SERS signal, which was also fed through a second-order Savitzky–Golay low-pass smoothing filter to remove high-frequency noise, is shown in black. (*D*) Superimposed data from patient 3 at 42 mW and 300 ms, and a SERS signal acquired at a concentration of 25 pM. (*Inset*) Extracted SERS signal after DCLS background cancellation. (*E*) Figure shows superimposed data from patient 3 at 15 mW and 1 s, and a SERS signal acquired at a concentration of 6 pM. (*Inset*) Extracted SERS signal after DCLS background cancellation. (*F*) Simulated data from patient 3 at 42 mW and 300 ms, and a SERS signal acquired at a concentration of 6 pM. (*Inset*) Extracted SERS signal after DCLS background cancellation. (*G*) Raman signal extracted from superimposed data at varying concentrations. The signal was evaluated over 90 acquisitions from patient 3 at 15 mW and 1 s. At 6 pM, the signal was well above background. (*H*) Raman signal extracted from superimposed data at varying concentrations. The signal was evaluated over 90 acquisitions from patient 3 at 42 mW and 300 ms. At 6 pM, the signal was well above background.

Label-free Raman point spectroscopy, on the other hand, has the capability to detect intrinsic molecular changes sensitively at the earliest stages of cancer formation without the use of any molecular imaging probes. Its ability to identify unique spectral fingerprints associated with cancerous tissues has resulted in 100% sensitivity, 89% specificity, and 95% accuracy for differentiation between normal colon and hyperplastic and adenomatous polyps (28). Although this technique of looking at intrinsic molecular differences between normal and cancerous tissues shows great potential for clinical use, its biggest limitation lies in the weak signal associated with spontaneous Raman scattering and the inherent small field of view that limit it as a screening tool. As stated earlier, only a very small fraction of photons are inelastically scattered spontaneously, often resulting in tissue Raman signals much weaker than autofluorescence that can be masked by the broad-band fluorescence background. To compensate, high-power irradiation (that exceeds ANSI standards) and long exposure times are needed to acquire noisy signals that are often suboptimal. As a result of the long exposure time, reproducibility can be jeopardized due to the variability in users and the pressure they apply to the contact probe against the tissue surface.

To address the problem of weak Raman scattering and to provide molecular specificity for cancer, we have developed a unique strategy that uses silica/gold nanoparticles and the SERS effect, a phenomenon that increases the effective Raman scattered light by several orders of magnitude, as described earlier (14). Additionally, instead of looking at the weak intrinsic signal of the colon tissue itself, we intend to interrogate molecular markers of cancer by combining these bright SERS nanoparticles with antibodies or peptides directed against tumor-related or tumor-specific antigens. We intend to harness the ultrasensitive detection and multiplexing properties of Raman spectroscopy (6) and to combine those properties with specific molecular targeting moieties to improve early cancer detection by using a functional approach rather than a purely structural one.

Only two other groups, to our knowledge, have developed a fiber-based, noncontact Raman endoscope to interrogate SERS nanoparticles as contrast agents. Mohs et al. (29) describe a handheld Raman probe that is able to achieve similar femtomolar sensitivity to our system. However, their system uses a high-powered laser (200 mW) and relatively long integration times (up to 10 s) for detection. These settings are not suitable for clinical translation because they exceed the MPE limits established by ANSI, and these features will prevent, or limit, use in patients. Our system, on the other hand, was specifically designed for clinical use and falls below the MPE limits set forth by ANSI, using a maximum laser power of 42 mW with 300-ms integration times. An additional unique feature of our system is its capability of detecting up to 10 SERS flavors simultaneously. Furthermore, our Raman endoscope is designed for efficient use over a wide range of working distances to accommodate for imperfect positioning during endoscopy and the varying surface topology of human tissue. Wilson and colleagues (30, 31) describe a Raman system as well. However, they do not demonstrate multiplexing capabilities of their device, and their sensitivity levels were reported in the picomolar range (30, 31), whereas for the current work, the sensitivity levels are in the femtomolar range.

To date, the use of Raman nanoparticles as imaging contrast agents for clinical utility has never been demonstrated; however, several preclinical studies have recently shown much promise for their translation. Our group has recently demonstrated effective tumor targeting with the same SERS nanoparticles used to characterize our newly developed Raman endoscope, as discussed in this paper. Tumor targeting was achieved in various mouse models after either i.v. or topical administration. One approach we recently reported on involves the ability of Raman spectroscopy to identify the specific accumulation of these SERS nanoparticles in brain tumors after i.v. injection via the enhanced permeability and retention effect. It also shows the ability of these SERS nanoparticles to accumulate in the distant fingerlike protrusions from the main tumor sites, which could be very useful during brain tumor resection (13). Another approach we have reported on discusses the ability of these SERS nanoparticles to be functionalized with epidermal growth factor receptor (EGFR) affibodies and preferentially target EGFR-positive cell line A431 in both cell culture and a mouse model. In this study, a topical application approach was used, where the tumors grown on a mouse were excised and immediately exposed to functionalized SERS with EGFR affibody bound to the surface. Signals from A431 tumors were 34.7-fold higher vs. negative tumors and were significant ($P < 0.05$), suggesting that the tumor-targeted SERS nanoparticles specifically label the EGFRs in biological specimens (12). Based on measurements of the detection limit for our Raman device (2.2 amol or 1.3 million nanoparticles), we estimate that only a few hundred nanoparticles bound to each cell will be sufficient for detection with our system (a calculation is provided in *SI Appendix, SI Methods*). To compare with existing fluorescence imaging endoscopes, we can interpret the detection limit in terms of quantity of targeting molecules imaged; with about 400 targeting ligands conjugated to each nanoparticle, our device can detect <1 fmol of target receptor. By comparison, a recently reported fluorescence endoscope has a detection limit in the tens to hundreds of femtomoles (25). Various types of other Raman-based nanoparticles have also been evaluated for tumor-targeting efficiency, with each conjugated with its own targeting moieties, including EGFR antibodies (10) and arginine-glycine-aspartic acid (RGD) peptides (11); all show effective targeting to their respective tumor targets. One group has successfully demonstrated the ability to localize the sentinel lymph node after an intradermal injection of bimodal fluorescence-SERS gold nanorods into the forepaw of a mouse (32). Another multimodal imaging approach has been demonstrated using MRI and Raman spectroscopy in conjunction with SERS nanoparticles (33). Finally, theranostic Raman nanoparticles have recently been evaluated preclinically with an additional photothermal heating component for therapy (34).

Given that more nanoparticle constructs have been approved recently for clinical use, a major concern within the biomedical community has been the issue of their potential toxicity. As a result, several investigators have reported on the toxic effects of various nanoparticles after i.v. administration (35–41). Although most of these nanoparticles have a short circulating half-life, some reports have claimed that certain nanoparticles remain in the body for at least several months, particularly in the mononuclear phagocytic system (liver and spleen) (38, 42–44). To circumvent these toxicity issues, we intend to apply our tumor-targeting Raman nanoparticles topically onto the colonic epithelium; this could be done during routine colonoscopy. We have recently published several articles describing the biodistribution and toxicity effects of our Raman nanoparticles after being administered intrarectally (i.r.) vs. i.v. in mice (18, 22, 45) These extensive toxicity studies, using over 120 mice, revealed that after i.r. administration, the Raman nanoparticles remained localized in the colon, with the majority clearing after 24 h. Additionally, the i.r.-administered Raman nanoparticles never crossed over into the systemic circulation, as opposed to the mice injected i.v., where the Raman nanoparticles quickly accumulated in the liver and spleen with prolonged/indefinite retention. This localized route of administration will not only significantly decrease toxicity but may potentially increase effective targeting to the tumor. Several nanoparticle constructs, particularly larger ones, suffer from poor extravasation, making it very difficult for the conjugated nanoparticle to reach its target on the tumor itself (46). Our topical strategy avoids these complicated extravasation kinetics by being administered directly to the area of interest and presumably increasing the chance of our targeted nanoparticle reaching the cancerous or dysplastic lesion.

Although using Raman spectroscopy as a point detection device can offer valuable functional and molecular information, one drawback remains the inability to interrogate larger tissue surfaces and capture an image. Point detection Raman spectroscopy is limited to the spot size of the illumination fiber (~1 mm), only allowing for the interrogation of small tissue areas. Therefore, this technique is probably best suited for obtaining important molecular information after suspicious areas have been identified through white-light imaging, offering only an incremental advantage without screening capabilities. To address this limitation, we have already begun developing a second-generation Raman endoscope device, with a motorized rotational component that would have the ability to acquire an intensity map of the surface of the colon by stitching spectra together, hence forming an image, in a period that is consistent with the clinical paradigm.

It should be noted that although the colon is where we intend to focus our efforts initially to demonstrate our unique early detection strategy, this technique could be applied to other tissues that are accessible with an endoscopic device, including skin, bladder, stomach, lungs, esophagus, cervix, and vagina. Intraoperative strategies can also be an important area of application for this approach. With the discovery of new cancer biomarkers, corresponding new molecular targeting moieties can be developed and exploited for improved tumor specificity (26, 47, 48). Moreover, to improve early cancer detection further, one could couple the inherently good specificity associated with acquiring intrinsic Raman signal from cancerous tissues with the unparalleled sensitivity and multiplexing capabilities offered by using tumor-targeted SERS nanoparticles as contrast agents. This, in addition to further development on the instrumentation side, could lead to improved early cancer detection, with the hope of ultimately affecting patient outcome.

## Methods

**DCLS-Weighting Factors.** To accomplish unmixing, the DCLS method, also called the linear unmixing method, was used. This algorithm compares the acquired signal with known reference spectra, representative background spectra, and a freely varying polynomial component. The representative background spectrum is included as a reference spectrum in our analysis, and it is free to vary in magnitude for each measurement (49). The output of the DCLS algorithm is a magnitude of its extracted spectrum relative to its respective reference spectrum. The SERS nanotags that were used to obtain the reference spectra were provided by Cabot Security Materials (formerly Oxonica Materials).

**SERS Concentration Assessment.** Stock solutions of the SERS nanoparticles were diluted to the desired concentration. The concentrations were verified by analyzing them in a spectrophotometer (Evolution60; Thermo Scientific) at a wavelength of 538 nm, which is the wavelength at which the absorption of gold is the strongest. Because the SERS nanoparticles have a gold core, the absorption measured by the spectrophotometer is proportional to the number of the SERS nanoparticles present. The absorption readings were then converted to an equivalent concentration based on several data points of known concentration and absorbance readings. Unless otherwise noted, the concentration of SERS nanoparticles used for the majority of the characterization and multiplexing experiments was at ~1 nM.

**Mapping and Image Processing.** To take mapped images of a particular sample an *x/y/z* motorized stage was incorporated into the system. The stage (H101A ProScan Upright Microscope Stage; Prior Scientific) and stage control system (Prior ProScan Motorized Stage System; Prior Scientific) were controlled with a personal computer. Using MATLAB 7.5 R2007b (MathWorks), commands are sent to the stage control system through serial port communication. The stage control system moves the stage to the appropriate *x–y* coordinates and then sends a trigger signal to the CCD. The CCD then triggers the shutter control system, which opens the shutter, before the CCD acquires an FVB signal. The shutter requires 1 ms to open and 1.5 ms to close. Once the signal is acquired, the CCD sends another transistor-transistor logic (TTL) signal to the shutter control system to close the shutter. In this way, the stage, CCD signal acquisition, and shutter were all synchronized. Each CCD acquisition is saved and tagged with the respective *x–y* coordinate at which it was acquired. The acquisitions are then converted to a weighting factor using the DCLS algorithm and stored in a matrix, where each element of the matrix represents a pixel corresponding to the *x–y* coordinate at which the signal was acquired (49). The matrix of weighting factors was then plotted as an image that is scaled to make use of the full 32-bit grayscale range. Using Amide medical imaging data software (50), a Gaussian blur was applied to the mapped image to give it smooth contours. Each SERS flavor-weighting factor was then assigned a particular color. More information on image analysis is provided in *SI Appendix* (*Image Analysis*).

**Depth Study.** An agarose phantom was used to evaluate the maximum depth of penetration achieved using our newly developed Raman endoscope. The phantom was designed to mimic tissue absorption and scattering in the colon. It consisted of 1% agarose mixed with India ink to mimic colon tissue absorption at 785 nm. The final agarose solution had an optical absorbance of 1.25 $cm^{-1}$; the absorption of colon tissue is ~1.0 $cm^{-1}$. Liposyn 0.5% was used to mimic colon tissue scattering; the scattering coefficient of colon tissue is 7 $cm^{-1}$ (51). More details are provided in *SI Appendix* (*Depth Study*).

**Well Plate Experiment.** The well plates have a well depth of 10.67 mm and can hold a total volume of 370 μL. The wells were filled with S440 of varying concentration to a well height of ~9 mm by filling them with 300 μL of each concentration. The probe was fixed above the well at a height of about 3 mm above the well plate surface. The samples in the well were mixed with a pipette before signal acquisition to ensure that none of the SERS particles settled to the bottom of the well. To demonstrate the linearity of the concentration to Raman signal, a single acquisition was taken in each well. For this experiment, the following concentrations of S440 were used: 250, 125, 63, 31, 16, 8, 4, 2, 1, and 0.5 pM. To demonstrate the limit of detection, 25 acquisitions were taken for each well and the sensitivity was calculated. For this experiment, the following concentrations of S440 were used: 709, 632, 517, 440, and 326 fM.

**Defining Thresholds.** For the well plate sensitivity, depth of penetration, and scavenger hunt experiments, thresholds were created to differentiate a "true" signal from the background. The threshold was determined by averaging the weighting factors of a sample set of background signals plus a multiple of the SD. The *x* axis was plotted to show the multiple of the SD that was used. In the case of the well plate sensitivity study, the background used was MES buffer. MES buffer was placed in 10 wells and 25 acquisitions were taken per well, for a total sample set of 250 background acquisitions. The 250 background acquisitions were used to determine the average background signal and SD of the background signal. In the case of the depth of penetration study, the background used was the agarose solution. Ten random spots of the agarose solution were selected and 25 signals were acquired at each spot, for a total background sample set of 250 acquisitions.

In the case of the scavenger hunt study, the background signal was the signal acquired on ex vivo porcine colon tissue in which no SERS particles were present. Ten random spots of the porcine tissue were selected and a single signal was acquired at each spot, for a total background sample set of 10 acquisitions. The threshold was determined by averaging the weighting factors of a sample set of background signals plus a multiple of the SD.

**Statistical Analysis.** For the well plate sensitivity study, where the Raman device was pointed at a certain concentration of S440, the sensitivity was calculated by Sensitivity = $\frac{TP}{TP+FN} = \frac{TP}{n}$, where a true-positive result (*TP*) was defined as a weighting factor for S440 that was greater than the defined threshold. For the well plate experiment, 25 acquisitions were acquired per well (i.e., per concentration). Similarly, for the depth of penetration study, 25 acquisitions were acquired for each depth.

For the scavenger hunt, for a given threshold, the overall sensitivity for each user was given by $Sensitivity = \frac{TP\ of\ all\ combinations}{TP\ of\ all\ combinations\ +\ FN\ of\ all\ combinations}$ and the specificity was given by $Specificity = \frac{TN\ of\ all\ combinations}{TN\ of\ all\ combinations\ +\ FP\ of\ all\ combinations}$, where *TN* is a true-negative result and *FP* is a false-positive result (Fig. 5*C*). The classification rate (*CR*) is also referred to as the user accuracy and is given by $\frac{TN+TP}{TN+FP+FN+TP}$, where *TN*, *TP*, and *FP* are evaluated for all combinations. The misclassification rate (*Mis-CR*) is given by *Mis-CR = 1 − CR* (Fig. 5*C*). The combined user accuracy was evaluated by averaging the *CR* for all three users (Fig. 5*C*). The sensitivity, specificity, and *FP* rate of each flavor were also evaluated. The sensitivity for each flavor was given by $Sensitivity_{flavor,i} = \frac{TP_{flavor,i}}{TP_{flavor,i}+FN_{flavor,i}}$ (*SI Appendix*, Fig. 11), and the specificity for each flavor was given by $Specificity_{flavor,i} = \frac{TN_{flavor,i}}{TN_{flavor,i}+FP_{flavor,i}}$ (*SI Appendix*, Fig. 11), where *i* is the sample set of SERS flavors $i = \{S440, S481, S420, S421\}$.

Detailed information on methods used for clinical studies is provided in *SI Appendix* (*Clinical Background Cancellation* and *Clinical SERS Simulations*).

**ACKNOWLEDGMENTS.** This work was funded, in part, by National Cancer Institute (NCI) Network for Translational Research (NTR) Grant U54 CA136465 (to C.H.C. and S.S.G.) and by NCI Centers of Cancer Nanotechnology Excellence (CCNE) Grant U54 CA119367 (to S.S.G.), National Institute of Biomedical Imaging Grant BRP 5-R01-EBB000312 (to S.S.G.), In Vivo Cellular and Molecular Imaging Centers Grant P50 CA114747 (to S.S.G.), the Canary Foundation (S.S.G.), and the Chambers Family Foundation (C.H.C.). C.L.Z. was supported, in part, by a Research Supplement to Promote Diversity in Health-Related Research through CCNE Grant U54 CA119367.

1. Raman CV (1928) A new radiation. *Indian J Phys* 2:387–398.
2. Chan JW, et al. (2006) Micro-Raman spectroscopy detects individual neoplastic and normal hematopoietic cells. *Biophys J* 90(2):648–656.
3. Crow P, et al. (2005) Assessment of fiberoptic near-infrared raman spectroscopy for diagnosis of bladder and prostate cancer. *Urology* 65(6):1126–1130.
4. Kanter EM, et al. (2009) Application of Raman spectroscopy for cervical dysplasia diagnosis. *J Biophotonics* 2(1-2):81–90.
5. Kendall C, et al. (2009) Vibrational spectroscopy: A clinical tool for cancer diagnostics. *Analyst (Lond)* 134(6):1029–1045.
6. Keren S, et al. (2008) Noninvasive molecular imaging of small living subjects using Raman spectroscopy. *Proc Natl Acad Sci USA* 105(15):5844–5849.
7. Kirsch M, Schackert G, Salzer R, Krafft C (2010) Raman spectroscopic imaging for in vivo detection of cerebral brain metastases. *Anal Bioanal Chem* 398(4):1707–1713.
8. Petibois C (2010) Imaging methods for elemental, chemical, molecular, and morphological analyses of single cells. *Anal Bioanal Chem* 397(6):2051–2065.
9. Pijanka JK, et al. (2010) Vibrational spectroscopy differentiates between multipotent and pluripotent stem cells. *Analyst (Lond)* 135(12):3126–3132.
10. Qian X, et al. (2008) In vivo tumor targeting and spectroscopic detection with surface-enhanced Raman nanoparticle tags. *Nat Biotechnol* 26(1):83–90.
11. Zavaleta C, et al. (2008) Noninvasive Raman spectroscopy in living mice for evaluation of tumor targeting with carbon nanotubes. *Nano Lett* 8(9):2800–2805.
12. Jokerst JV, Miao Z, Zavaleta C, Cheng Z, Gambhir SS (2011) Affibody-functionalized gold-silica nanoparticles for Raman molecular imaging of the epidermal growth factor receptor. *Small* 7(5):625–633.
13. Kircher MF, et al. (2012) A brain tumor molecular imaging strategy using a new triple-modality MRI-photoacoustic-Raman nanoparticle. *Nat Med* 18(5):829–834.
14. Fleischmann M, Hendra PJ, McQuillan AJ (1974) Raman spectra of pyridine adsorbed at a silver electrode. *Chem Phys Lett* 26(2):163–166.
15. Levin B, et al.; American Cancer Society Colorectal Cancer Advisory Group; US Multi-Society Task Force; American College of Radiology Colon Cancer Committee (2008) Screening and surveillance for the early detection of colorectal cancer and adenomatous polyps, 2008: A joint guideline from the American Cancer Society, the US Multi-Society Task Force on Colorectal Cancer, and the American College of Radiology. *Gastroenterology* 134(5):1570–1595.
16. Stallmach A, Schmidt C, Watson A, Kiesslich R (2011) An unmet medical need: Advances in endoscopic imaging of colorectal neoplasia. *J Biophotonics* 4(7-8):482–489.
17. Soetikno RM, et al. (2008) Prevalence of nonpolypoid (flat and depressed) colorectal neoplasms in asymptomatic and symptomatic adults. *JAMA* 299(9):1027–1035.
18. Thakor AS, et al. (2011) The fate and toxicity of Raman-active silica-gold nanoparticles in mice. *Sci Transl Med* 3(79):79ra33.
19. Doering WE, Piotti ME, Natan MJ, Freeman RG (2007) SERS as a foundation for nanoscale, optically detected biological labels. *Adv Mater* 19(20):3100–3108.
20. Sha MY, Xu H, Natan MJ, Cromer R (2008) Surface-enhanced Raman scattering tags for rapid and homogeneous detection of circulating tumor cells in the presence of human whole blood. *J Am Chem Soc* 130(51):17214–17215.
21. Zavaleta CL, et al. (2009) Multiplexed imaging of surface enhanced Raman scattering nanotags in living mice using noninvasive Raman spectroscopy. *Proc Natl Acad Sci USA* 106(32):13511–13516.
22. Zavaleta CL, et al. (2011) Preclinical evaluation of Raman nanoparticle biodistribution for their potential use in clinical endoscopy imaging. *Small* 7(15):2232–2240.
23. Dacosta RS, Wilson BC, Marcon NE (2002) New optical technologies for earlier endoscopic diagnosis of premalignant gastrointestinal lesions. *J Gastroenterol Hepatol* 17(Suppl):S85–S104.
24. DaCosta RS, Wilson BC, Marcon NE (2005) Optical techniques for the endoscopic detection of dysplastic colonic lesions. *Curr Opin Gastroenterol* 21(1):70–79.
25. Funovics MA, Alencar H, Montet X, Weissleder R, Mahmood U (2006) Simultaneous fluorescence imaging of protease expression and vascularity during murine colonoscopy for colonic lesion characterization. *Gastrointest Endosc* 64(4):589–597.
26. Hsiung PL, et al. (2008) Detection of colonic dysplasia in vivo using a targeted heptapeptide and confocal microendoscopy. *Nat Med* 14(4):454–458.
27. Uddin MJ, et al. (2010) Selective visualization of cyclooxygenase-2 in inflammation and cancer by targeted fluorescent imaging agents. *Cancer Res* 70(9):3618–3627.
28. Molckovsky A, Song LM, Shim MG, Marcon NE, Wilson BC (2003) Diagnostic potential of near-infrared Raman spectroscopy in the colon: Differentiating adenomatous from hyperplastic polyps. *Gastrointest Endosc* 57(3):396–402.
29. Mohs AM, et al. (2010) Hand-held Spectroscopic Device for In Vivo and Intraoperative Tumor Detection: Contrast Enhancement, Detection Sensitivity, and Tissue Penetration. *Anal Chem* 82(21):9058–9065.
30. Mallia RJ, McVeigh PZ, Veilleux I, Wilson BC (2012) Filter-based method for background removal in high-sensitivity wide-field-surface-enhanced Raman scattering imaging in vivo. *J Biomed Opt* 17(7):076017.
31. McVeigh PZ, Mallia RJ, Veillieux I, Wilson BC (2012) Development of widefield SERS imaging endoscope. *Proc SPIE* 8217:821704.
32. Qian J, Jiang L, Cai F, Wang D, He S (2011) Fluorescence-surface enhanced Raman scattering co-functionalized gold nanorods as near-infrared probes for purely optical in vivo imaging. *Biomaterials* 32(6):1601–1610.
33. Yigit MV, et al. (2011) Noninvasive MRI-SERS imaging in living mice using an innately bimodal nanomaterial. *ACS Nano* 5(2):1056–1066.
34. von Maltzahn G, et al. (2009) SERS-Coded Gold Nanorods as a Multifunctional Platform for Densely Multiplexed Near-Infrared Imaging and Photothermal Heating. *Adv Mater* 21(31):3175–3180.
35. Adiseshaiah PP, Hall JB, McNeil SE (2010) Nanomaterial standards for efficacy and toxicity assessment. *Wiley Interdiscip Rev Nanomed Nanobiotechnol* 2(1):99–112.
36. Dobrovolskaia MA, McNeil SE (2007) Immunological properties of engineered nanomaterials. *Nat Nanotechnol* 2(8):469–478.
37. McNeil SE (2009) Nanoparticle therapeutics: A personal perspective. *Wiley Interdiscip Rev Nanomed Nanobiotechnol* 1(3):264–271.
38. Schipper ML, et al. (2008) A pilot toxicology study of single-walled carbon nanotubes in a small sample of mice. *Nat Nanotechnol* 3(4):216–221.
39. Stern ST, McNeil SE (2008) Nanotechnology safety concerns revisited. *Toxicol Sci* 101(1):4–21.
40. Xie G, Sun J, Zhong G, Shi L, Zhang D (2009) Biodistribution and toxicity of intravenously administered silica nanoparticles in mice. *Arch Toxicol* 84(3):183–190.
41. Yong KT, Roy I, Ding H, Bergey EJ, Prasad PN (2009) Biocompatible near-infrared quantum dots as ultrasensitive probes for long-term in vivo imaging applications. *Small* 5(17):1997–2004.
42. Balasubramanian SK, et al. (2010) Biodistribution of gold nanoparticles and gene expression changes in the liver and spleen after intravenous administration in rats. *Biomaterials* 31(8):2034–2042.
43. Goel R, Shah N, Visaria R, Paciotti GF, Bischof JC (2009) Biodistribution of TNF-alpha-coated gold nanoparticles in an in vivo model system. *Nanomedicine (Lond)* 4(4):401–410.
44. Lin P, et al. (2008) Computational and ultrastructural toxicology of a nanoparticle, Quantum Dot 705, in mice. *Environ Sci Technol* 42(16):6264–6270.
45. Thakor AS, et al. (2011) Oxidative stress mediates the effects of Raman-active gold nanoparticles in human cells. *Small* 7(1):126–136.
46. Smith BR, Cheng Z, De A, Rosenberg J, Gambhir SS (2010) Dynamic visualization of RGD-quantum dot binding to tumor neovasculature and extravasation in multiple living mouse models using intravital microscopy. *Small* 6(20):2222–2229.
47. de Wit M, et al. (2012) Cell surface proteomics identifies glucose transporter type 1 and prion protein as candidate biomarkers for colorectal adenoma-to-carcinoma progression. *Gut* 61(6):855–864.
48. Ginty F, et al. (2008) The relative distribution of membranous and cytoplasmic met is a prognostic indicator in stage I and II colon cancer. *Clin Cancer Res* 14(12):3814–3822.
49. Lutz BR, et al. (2008) Spectral analysis of multiplex Raman probe signatures. *ACS Nano* 2(11):2306–2314.
50. Loening AM, Gambhir SS (2003) AMIDE: A free software tool for multimodality medical image analysis. *Mol Imaging* 2(3):131–137.
51. Marchesini R, et al. (1994) Ex vivo optical properties of human colon tissue. *Lasers Surg Med* 15(4):351–357.